Dynamics-based estimates of decline trend with fine temporal variations in China's $PM_{2.5}$ emissions

Zhen Peng[1]†, Lili Lei[1,2]†, Zhe-Min Tan[1,2*], Meigen Zhang[3*], Aijun Ding[1] and Xingxia Kou[4]

[1]School of Atmospheric Sciences, Nanjing University, Nanjing 210093, China

[2]Key Laboratory of Mesoscale Severe Weather, Ministry of Education, Nanjing University, Nanjing 210093, China

[3]State Key Laboratory of Atmospheric Boundary Layer Physics and Atmospheric Chemistry, Institute of Atmospheric Physics, Chinese Academy of Sciences, Beijing 100029, China

[4]Institute of Urban Meteorology, China Meteorological Administration, Beijing 100089, China

Corresponding author: Zhe-Min Tan (zmtan@nju.edu.cn) and Meigen Zhang (mgzhang@mail.iap.ac.cn)

Abstract

Timely, continuous, and dynamics-based estimates of $PM_{2.5}$ emissions with a high temporal resolution can be objectively and optimally obtained by assimilating observed surface $PM_{2.5}$ concentrations using flow-dependent error statistics. The annual dynamics-based estimates of $PM_{2.5}$ emission averaged over mainland China for years 2016-2020 without biomass burning emissions are 7.66, 7.40, 7.02, 6.62 and 6.38 Tg, respectively, which are very closed to the values of MEIC. Annual $PM_{2.5}$ emissions in China have consistently decreased of approximately 3% to 5% from 2017 to 2020. Significant $PM_{2.5}$ emission reductions occurred frequently in regions with large $PM_{2.5}$ emissions. COVID-19 could cause a significant reduction of $PM_{2.5}$ emissions in the north China plain and northeast of China in 2020. The magnitudes of $PM_{2.5}$ emissions were greater in the winter than in the summer. $PM_{2.5}$ emissions show an obvious diurnal variation that varies significantly with the season and urban population. Compared to the diurnal variations of $PM_{2.5}$

emission fractions estimated based on diurnal variation profiles from US and EU, the estimated $PM_{2.5}$ emission fractions are 1.25% larger during the evening, the morning peak is 0.57% smaller in winter and 1.05% larger in summer, and the evening peak is 0.83% smaller. Improved representations of $PM_{2.5}$ emissions across time scales can benefit emission inventory, regulation policy and emission trading schemes, particularly for especially for high temporal resolution air quality forecasting and policy response to severe haze pollutions or rare human events with significant socioeconomic impacts.

1. Introduction

Anthropogenic emissions have imposed essential influences on the earth system, from hourly air quality and human health to long-time climate and environment. To reduce anthropogenic emissions, the Chinese government has enforced the Clean Air Action (2013) since 2013. Studies to date that evaluated the emission controls and understood the climate responses from emission reductions often have used either a fixed meteorology with emission changes or *vice versa* (Li et al., 2019a; Li et al., 2021, Zhai et al., 2021). Estimated emissions from empirical extrapolation were commonly applied to analyze the meteorological-chemical mechanisms and associated social-economic impacts from occasional events like the 2015 China Victory Day Parade and Coronavirus Disease 2019 (COVID-19) pandemic (Wang et al., 2017; Liu et al., 2020; Huang et al., 2020; Zhu et al., 2021). But to better understand both long-term and short-term influences from emission changes, the continuous, up-to-date, and high temporal-/spatial-resolution emission estimates with coherent interactions of meteorology and emission changes are needed.

The complex contributions from energy production, industrial processes, transportation, and residential consumptions have imposed great challenges to accurately estimate the emissions. The emission inventories created by the traditional bottom-up techniques were typically outdated from the present day due to the lack of accurate and timely statistics, and often with coarse temporal resolutions from monthly to annual (Zhang et al., 2009; Li et al., 2014; Janssens-Maenhout et al., 2015; Zheng et al., 2018). Alternatively, update-to-date emission estimates with high temporal-spatial resolutions could be provided by top-down techniques (Miyazaki et al., 2017), but most emissions estimated by top-down techniques were intermittent and analyzed at

monthly scale or longer longer (Zhang et al., 2016; Jiang et al., 2017; Qu et al., 2017; Cao et al., 2018; Müller et al., 2018; Chen et al., 2019; Li et al., 2019b; Miyazaki et al., 2020). Moreover, emissions updated by the top-down techniques based on satellite observations could be insufficient to capture realistic near-surface characteristics (Li et al., 2019b; Liu et al., 2011; Choi et al., 2020).

Given the development of observation networks and advanced data assimilation strategies, timely and dynamics-based emission estimates with high temporal resolution can be achieved by harmonically constraining the atmospheric-chemical model with dense observations of trace gas compounds through an optimal assimilation methodology. The ensemble Kaman smoother (EnKS) (Whitaker et al., 2002; Peters et al., 2007; Peng et al., 2015), as a four-dimensional (4D) assimilation algorithm, makes use of chemical observations from past to future to provide an optimal estimate of source emissions, and it can capture the "error of the day" and construct fine emission characteristics with high temporal-spatial resolutions by using short-term ensemble forecasts (Kalnay, 2002). Since 2013, the fine particulate matter pollution ($PM_{2.5}$, particles smaller than 2.5 μm in diameter) as the most urgent threat to public health has been persistently decreased, and ground-based observations of $PM_{2.5}$ have been progressively increased (Huang et al., 2018). Thus by harmonically assimilating dense surface $PM_{2.5}$ observations into an atmospheric-chemical model through an EnKS, hourly estimates of $PM_{2.5}$ emission that were continuously cycled for years 2016-2020 are presented in this study.

The timely estimated emissions can provide guidance for emission inventories that usually have time lags and emission trading schemes that often require up-to-date source emissions. Based on the dynamics-based estimated emissions with harmonic combination of the model and observations, better evaluation of the emission controls and more comprehensive understanding of the consequent climate responses can be obtained. The high temporal-resolution estimated emissions can reveal features of emissions that are absent from the traditional ones with coarse temporal resolutions. Moreover, the timely and dynamics-based emission estimates with high temporal resolution are essential for regional air quality modeling, especially for the occurrence of severe haze pollutions associated with timely evaluation for the impact on public health (Attri et al., 2001; Wang et al., 2014; Ji et al., 2018; Wang et al., 2020; Liu et al., 2021) and events that lead to large changes of emissions and significant socioeconomic impacts such as the COVID-19 pandemic (Huang et al., 2020; Le et al., 2020).

2. Data assimilation and experimental design

The estimate of $PM_{2.5}$ emission can be successfully constrained by the $PM_{2.5}$ concentration observations through an ensemble Kalman filter (EnKF; Peng et al., 2017, 2018, 2020). For a retrospective 'reanalysis' mode here, all available $PM_{2.5}$ concentration observations, including those data collected after the analysis time, can be used. Thus a EnKS, a direct generalization of the EnKF, is applied to incorporate $PM_{2.5}$ concentration observations both before and after the analysis time, aiming to provide an optimal estimate of the $PM_{2.5}$ emission. In simple words, The emissions are updated by current and future observations though EnKS, while the concentrations are updated by current observations though EnKF. Detailed procedures of the EnKS are described in section 2.1.

2.1 An ensemble Kalman smoother to update the source emission

The ensemble priors of source emissions $\mathbf{e}^f$ is created by multiplying a scaling factor $\boldsymbol{\lambda}^f$ to the prescribed emission $\mathbf{e}^{\mathbf{p}}$ (Peng et al., 2017, 2018, 2020), where the superscript *f* denotes priors. Given a time-invariant $\mathbf{e}^{\mathbf{p}}$, the update of $\mathbf{e}^f$ is equivalent to the update of $\boldsymbol{\lambda}^f$. Due to a time lag, the prior scaling factor at time *t*-1 ($\boldsymbol{\lambda}^f_{t-1}$) is updated by chemical observations at time *t* ($\mathbf{y}^c_t$). At time *t*-1, the prior scaling factor for the i^{th} member is written as

$$\boldsymbol{\lambda}^f_{i,t-1} = \frac{1}{M}\left[\left(\beta\frac{\mathbf{c}^f_{i,t-1}}{\overline{\mathbf{c}}^f_{t-1}} + 1 - \beta\right) + \sum_{j=t-M}^{t-2}\boldsymbol{\lambda}^a_{i,\,j|j+1:t-1}\right]. \quad (1)$$

The first term is the concentration ratio given by the prior of the chemical fields ($\mathbf{c}^f_{i,t-1}$) normalized by the ensemble mean ($\overline{\mathbf{c}}^f_{t-1}$), where β is an inflation factor used to compensate the insufficient ensemble spread (Peng et al., 2017). Through using the concentration ratio, each ensemble member of the source emissions naturally has the spatial correlations given by the chemical fields. The second term is the mean of the posterior scaling factors at previous assimilation cycles, where the superscript *a* denotes posteriors, *M* is the length of smoothing, and the subscript *j*+1:*t*-1 indicates that the scaling factor at time *j* is updated by future observations from *j*+1 to *t*-1. The assimilation of future observations will be described below.

The ensemble square-root filter (EnSRF) (Peng et al., 2017) is used to update $\boldsymbol{\lambda}_{t-1}^{f}$ by assimilating $\mathbf{y}_t^c$. For the scaling factor at time *t*-1, posterior ensemble mean is given by

$$\bar{\boldsymbol{\lambda}}_{t-1}^{a} = \bar{\boldsymbol{\lambda}}_{t-1}^{f} + \rho \circ \mathbf{P}_{t-1,t}^{ec} \mathbf{H}_t^{c\mathbf{T}} \left(\mathbf{H}_t^c \mathbf{P}_t^c \mathbf{H}_t^{c\mathbf{T}} + \mathbf{R}_t^c \right)^{-1} \left(\mathbf{y}_t^c - H_t^c \bar{\mathbf{c}}_t^f \right), \quad (2)$$

and posterior ensemble perturbations are given by

$$\boldsymbol{\lambda}_{i,t-1}^{'a} = \boldsymbol{\lambda}_{i,t-1}^{'f} - \rho \circ \mathbf{P}_{t-1,t}^{ec} \mathbf{H}_t^{c\mathbf{T}} \left[\left(\sqrt{\mathbf{H}_t^c \mathbf{P}_t^c \mathbf{H}_t^{c\mathbf{T}} + \mathbf{R}_t^c} \right)^{-1} \right]^{\mathbf{T}} \left[\sqrt{\left(\mathbf{H}_t^c \mathbf{P}_t^c \mathbf{H}_t^{c\mathbf{T}} + \mathbf{R}_t^c \right)} + \sqrt{\mathbf{R}_t^c} \right]^{-1} \mathbf{H}_t^c \boldsymbol{\lambda}_{i,t-1}^{'f}, \quad (3)$$

where $\mathbf{P}_{t-1,t}^{ec}$ denotes the background error covariance matrix of $\boldsymbol{\lambda}_{t-1}^{f}$ and $\mathbf{c}_t^f$, $\mathbf{P}_t^c$ indicates the background error covariance matrix of $\mathbf{c}_t^f$, H_t^c, $\mathbf{H}_t^c$ and $\mathbf{R}_t^c$ are the observation forward operator, Jacobian matrix and observation error covariance matrix of the chemical fields at time *t*, ρ is the localization matrix and $\circ$ denotes the Schur (elementwise) product.

By applying the ensemble Kalman smoother (EnKS) (Whitaker et al., 2002; Peters et al., 2007), the chemical observation $\mathbf{y}_t^c$ is also assimilated to update the posterior scaling factor at previous assimilation cycles $j\,(j = t-K,\ldots,t-2)$. After assimilating the future chemical observation at time *t*, posterior ensemble mean of the scaling factor at *j* is given by

$$\bar{\boldsymbol{\lambda}}_{j|j+1:t}^{a} = \bar{\boldsymbol{\lambda}}_{j|j+1:t-1}^{a} + \rho \circ \mathbf{P}_{j|j+1:t-1,t}^{ec} \mathbf{H}_t^{c\mathbf{T}} \left(\mathbf{H}_t^c \mathbf{P}_t^c \mathbf{H}_t^{c\mathbf{T}} + \mathbf{R}_t^c \right)^{-1} \left(\mathbf{y}_t^c - H_t^c \bar{\mathbf{c}}_t^f \right), \quad (4)$$

and posterior ensemble perturbations are given by

$$\boldsymbol{\lambda}_{i,j|j+1:t}^{'a} = \boldsymbol{\lambda}_{i,j|j+1:t-1}^{'a} - \rho \circ \mathbf{P}_{j|j+1:t-1,t}^{ec} \mathbf{H}_t^{c\mathbf{T}} \left[\left(\sqrt{\mathbf{H}_t^c \mathbf{P}_t^c \mathbf{H}_t^{c\mathbf{T}} + \mathbf{R}_t^c} \right)^{-1} \right]^{\mathbf{T}} \left[\sqrt{\left(\mathbf{H}_t^c \mathbf{P}_t^c \mathbf{H}_t^{c\mathbf{T}} + \mathbf{R}_t^c \right)} + \sqrt{\mathbf{R}_t^c} \right]^{-1} \mathbf{H}_t^c \boldsymbol{\lambda}_{i,t-1}^{'f}, \quad (5)$$

where $\mathbf{P}_{j|j+1:t-1,t}^{ec}$ denotes the background error covariance matrix of $\boldsymbol{\lambda}_{j|j+1:t-1}^{a}$ and $\mathbf{c}_t^f$. After (2)-(5), the updated $\boldsymbol{\lambda}_{j|j+1:t}^{a}$, $j\,(j = t-M+1,\ldots,t-1)$ will be used to construct the prior scaling factor at next time *t*+1 (1).

As a Monte Carlo approach, the EnKS uses the forecast-analysis error covariances based on ensemble forecasts / analyses to compute the Kalman gain matrix with time lags, to incorporate observations from the past to the future. The first iteration of EnKS is equivalent to EnKF that assimilates observations up to the analysis time. The following iterations of EnKS assimilate observations in the future to update the state at the analysis time. The hourly forecasts of $PM_{2.5}$ concentration from the cycling assimilation experiment matched the independent observed quantities (Figure 1). Therefore, the ability of EnKS to retrieve the source emissions has been demonstrated. Previous studies also showed that simulations forced by the posterior emissions could produce improved forecasts for $PM_{2.5}$, SO_2, and NO_2 than those with a priori emissions (Peng et al., 2020).

2.2 WRF-Chem model, observations and emissions

To simulate the transport of aerosol and chemical species, the WRF-Chem model version 3.6.1 (Grell et al., 2005) that has the meteorological and chemical components fully coupled is used. The model parameterization schemes follow Peng et al. (2017). Figure 2 shows the model domain that covers most east Asia regions. Horizontal grid spacing is 45 km with 57 vertical levels and model top at 10 hPa.

Experiments are conducted for each year from 2016 to 2020 separately. The 6-h meteorological observations, including all in-situ observations and cloud motion vectors from the National Centers for Environmental Prediction (NCEP) Global Data Assimilation System (GDAS; http://www.emc.ncep.noaa.gov/mmb/data_processing/prepbufr.doc/table_2.htm), are assimilated every 6 h. The hourly observed chemical quantities, which contain PM_{10}, $PM_{2.5}$, SO_2, NO_2, O_3, and CO from the Ministry of Ecology and Environment of China (https://aqicn.org/map/china/cn/), are assimilated every hour. Figure 2 shows the assimilated chemical observation network, which has 560 randomly chosen stations from 1576 stations in total. The thinning of observations is applied to avoid correlated errors of observations. The spatial autocorrelation of the thinning of observations is close to the original observations (Peng et al., 2017). The observation priors are computed by the "observer" portion of the Grid-point Statistical Interpolation system (GSI) (Kleist et al., 2009).

The hourly and time-invariantly prescribed anthropogenic emissions are obtained from the EDGAR-HTAP (Emission Database for Global Atmospheric Research for Hemispheric Transport

of Air Pollution v2.2) v2.2 inventory (Janssens-Maenhout et al., 2015), in which the Chinese emissions are derived from MEIC in 2010 (Lei et al., 2011; Li et al., 2014). Natural emissions, including the biogenic (Guenther et al., 1995), dust (Ginoux et al., 2001), dimethyl sulfide and sea salt emissions (Chin et al., 2000), are computed online.

2.3 Assimilation and ensemble configurations

The $PM_{2.5}$ emission directly gives the primary $PM_{2.5}$, and then the primary $PM_{2.5}$ along with other precursor emissions could contribute to the secondary $PM_{2.5}$. The observations of $PM_{2.5}$ concentrations that contain both primary and secondary $PM_{2.5}$, are used to constrain the $PM_{2.5}$ emission through data assimilation. Thus the correlations between the concentration observations and source emissions might be contaminated by the secondary $PM_{2.5}$. Since the secondary formation process can be captured by the WRF-Chem model, the impact of the secondary $PM_{2.5}$ is indirectly considered. The detailed updated state variables with the according observations follow Peng et al. (2018). The concentrations and emissions of $PM_{2.5}$~~, NH_3,~~ and $PM_{2.5}$ precursors (SO_2 and NO) that have observations ~~(SO_2 and NO),~~ are updated by the observed quantities, respectively.~~,~~ Besides, NH_3 concentrations and emissions are constrained by $PM_{2.5}$ observations, however,~~but~~ the VOC that are also $PM_{2.5}$ precursors are not updated due to the lack of direct and limited observations~~.~~. One possible way to untangle the impact of secondary $PM_{2.5}$ on the estimates of $PM_{2.5}$ emission is to jointly estimate the source emission, primary and secondary $PM_{2.5}$ given the concentration observations.

The National Oceanic and Atmospheric Administration (NOAA) operational EnKF system (https://dtcenter.ucar.edu/com-GSI/users/docs/users_guide/GSIUserGuide_v3.7.pdf), which is an EnSRF and modified with the EnKS feature, is used to assimilate the observations. Ensemble size is set to 50. To combat the sampling error resulted from a limited ensemble size, covariance localization and inflation are applied. The Gaspari and Cohn (GC) (1999) function with a length scale of 675 km is used to localize the impact of observations and mitigate the spurious error correlations between observations and state variables. The constant multiplicative posterior inflation (Whitaker and Hamill 2012) with coefficients 1.12 for all meteorological and chemical variables is applied to enlarge the ensemble spread. The inflation β for advancing the scale factor is 1.2. The smoothing length M for source emissions is 4, and the EnKS lagged length K is 6. The larger the K value, the more future observations are assimilated to constrain the current emission

192 estimate. But the sample estimated temporal correlations could be contaminated by sampling errors
193 and model errors, especially with increased lagged times. Thus, there is a tradeoff between the
194 amount of future observations and accuracy of sample estimated temporal correlations. The choice
195 of K (=6) is determined by sensitivity experiments.

196 At 0000 UTC 26 December of previous year, ensemble initial conditions (ICs) of the
197 meteorological fields are generated by adding random perturbations that sample the static
198 background error covariances (Barker et al., 2012) on the NCEP FNL (Final) analyses (Torn et al.,
199 2006). Ensemble ICs of the chemical fields are 0, and source emissions of each ensemble member
200 are adopted from the EDGAR-HTAP v2.2 inventory with random perturbations of mean 0 and
201 variances of 10% of the emission values. Hourly ensemble lateral boundary conditions (LBCs) are
202 generated using the same fixed-covariance perturbation technique as the ensemble ICs. After 6-d
203 spin up, ensemble data assimilation experiments start cycling for each year.

204 **3. $PM_{2.5}$ emission for years 2016-2020**

205 Starting from the time-invariant source emission PR2010 (Janssens-Maenhout et al., 2015),
206 the dynamics-based estimates of the $PM_{2.5}$ emissions are obtained, which include both the
207 contributions of the anthropogenic and biomass burning emissions. The mean annual $PM_{2.5}$
208 emissions from biomass burning in China (2003~2017) was 0.51 Tg (Yin et al., 2019). The annual
209 dynamics-based estimates of $PM_{2.5}$ emission (DEPE) averaged over mainland China for years
210 2016-2020 without biomass burning emissions are 7.66, 7.40, 7.02, 6.62 and 6.38 Tg, respectively.
211 The values from the Multi-resolution Emission Inventory (MEIC; Zheng et al., 2018) that does not
212 consider the contributions of biomass burning emissions, are 8.10, 7.60, 6.70, 6.38 and 6.04 Tg,
213 respectively. Thus the annual DEPE are very closed to the values of MEIC. From year 2017 to
214 2020, the estimated annual $PM_{2.5}$ emissions are reduced 3.4%, 8.4%, 13.6% and 16.7%
215 respectively compared to that of year 2016. There has been 3%-5% persistent reduction of annual
216 $PM_{2.5}$ emission from year 2017 to 2020, which demonstrates the effectiveness of China's Clean
217 Air Action (2013) implemented since 2013 and China Blue Sky Defense War Plan (2018) enforced
218 since 2018 with strengthened industrial emission standards, phased out outdated industrial
219 capacities, promoted clean fuels in residential sector and so on (Zhang et al., 2019).

220 The monthly DEPE show reduction of $PM_{2.5}$ emission nearly in each month from years
221 2016 to 2020 (Figure 3a), which further demonstates the effectiveness of China's national plan.

Compared to year 2016, both the reduction amount and reduction ratio of $PM_{2.5}$ emission are more prominent for February, March, June-September, and November than the other months (Figure3b). Given larger magnitudes of $PM_{2.5}$ emission in winter than in summer, emission controls with a focus from October to May should be considered in the design of future clean air actions in China, since total $PM_{2.5}$ emission during this period accounts for approximate 75% annual amount. Spatial distributions of the changes of $PM_{2.5}$ emission from year 2017 to 2020 compared to year 2016 show significant decreases occurred at Beijing-Tianjin-Hebei region (BTH), Yangtze River Delta region (YRD), Pearl River Delta region (PRD) and Sichuan-Chongqing Region (SCR), especially for years 2019-2020 (Figure 4). From year 2016 to 2020, BTH, YRD and SRC have larger reductions of $PM_{2.5}$ emission than PRD, but SCR has larger reduction ratio compared to year 2016 than BTH and YRD (Figure 5). Therefore, BTH and YRD have more potentials for $PM_{2.5}$ emission controls than PRD and SCR, which can give a guidance for future clean air actions. More specifically, most provinces have $PM_{2.5}$ emission reduction from year 2016 to 2020, and the reduction ratios generally increase from year 2017 to 2020 (Table 1), which confirms continuous and effective emission controls from Clean Air Action to Blue Sky Defense War Plan in China. The monthly DEPE also demonstates the effectiveness of strict implementations of emission reduction policies in China, such as the coal ban for residential heating since the 2017-2018 winter. There was a sharp change of $PM_{2.5}$ emission, from increase in 2017 to decrease in 2018. As shown by Figure 6, spatial distributions of the changes of $PM_{2.5}$ emissions in December compared to November in 2017 show obvious increases in most China. However, the changes in 2018 show significant decreases in areas of Beijing, Tianjin, Hebei, Shanxi, Henan and Anhui provinces due to the implementation of the coal ban.

Despites the trend in $PM_{2.5}$ emissions from year 2016 to 2020, the DEPE of year 2016 has similar monthly distributions to MEIC2016-2020 in general (Figure 3a). MEIC has a “Pan-shape” monthly distribution with nearly time-invariant $PM_{2.5}$ emissions from April to October. This seasonal dependence of emissions is mainly contributed by the variations of residential energy use, which are empirically dependent on coarse monthly mean temperature intervals and thus cannot reflect the realistic monthly variations (Streets et al., 2003; Li et al., 2017). The centralized heating system in North China has a fixed date of turning-on and turning-off during each heating season. Therefore, a sudden raise of emissions from October to November and a sudden drop of emissions from March to April are shown. But the turning-on and turning-off date are variable in different

regions, which imposes a smoothing impact on the emissions. However, the DEPE yet shows a "V-shape" monthly distribution, with the minimum occurring in August. The estimated $PM_{2.5}$ emission is 11.8% higher than MEIC2016 in April but 12.1% lower than MEIC2016 in August, and these different monthly distributions can influence the consequent climate responses including the radiative forcing and energy budget (Yang et al., 2020) and also impact the health issues (Liu et al., 2018). Moreover, monthly fractions of the DEPE are consistent cross years (Figure 3c). The absence of interannual variations of monthly $PM_{2.5}$ emission fraction provides basis for previous studies that follow the same monthly changes of source emissions from different years (Zhang et al., 2009; Zheng et al., 2020, 2021). Monthly allocations of $PM_{2.5}$ emission can be directly and objectively obtained given an estimated total annual amount based on the estimated monthly fractions of DEPE, which is valuable for emission inventory, air quality simulation, and potentially applications for future scenarios due to more accurate month fractions of DEPE. Since the hourly priors of $PM_{2.5}$ concentrations from the cycling assimilation for optimally estimating $PM_{2.5}$ emission fit to the observed $PM_{2.5}$ quantities (Figure 1), the monthly DEPE provides more realistic monthly fluctuations than the empirical estimate.

4. Diurnal variations of $PM_{2.5}$ emission

The DEPE with high temporal-resolution given the time-invariant prior PR2010 can reveal features that are unable to represent in the commonly used emission estimates. Although the prior PR2010 has no diurnal variations, hourly posteriors of $PM_{2.5}$ emission provide the first objectively estimated diurnal variations for different seasons for years 2016-2020. However, these estimated diurnal variations include the contributions of the time-varying boundary layer. An observing system simulation experiment (OSSE) is performed to investigate the effects of the boundary layer from 0000 UTC 29 December to 0006 UTC 1 February 2016. Details of this OSSE are presented in Appendix. The results indicate that the magnitude of posterior $PM_{2.5}$ emission from the OSSE is closer to the true emission than the prior. Since we have hourly assimilated observations to simultaneously update the chemical concentrations and source emissions, the impacts of time-varying boundary layer on the posterior $PM_{2.5}$ emissions are limited (Figures S1). A little larger estimated $PM_{2.5}$ emission fractions occurred in the morning and smaller estimated $PM_{2.5}$ emission fractions occurred in the afternoon, comparing to the time-invariant true emission. Nevertheless, the influences of time-varying boundary layer are still important to $PM_{2.5}$ emission estimates. To

283 statistically present the diurnal variations, the fractions of hourly $PM_{2.5}$ emissions divided by the
284 daily amount are averaged over different years and regions after excluding the impacts of time-
285 varying boundary layer based on the short-term period simulation, although the influences of
286 boundary layer could strongly vary with seasons or years (Figures 7 and 8, and Table 2). The
287 diurnal variations of $PM_{2.5}$ emission are critical for understanding the mechanisms of $PM_{2.5}$
288 formation and evolution and are also essential for $PM_{2.5}$ simulation and forecast.

289 Five-year mean diurnal variations of the estimated $PM_{2.5}$ emission fraction for mainland
290 China show that despite the monthly variations of $PM_{2.5}$ emission, the diurnal-variation fractions
291 for November, December, January and February are similar, while those for June, July and August
292 are similar (Figure 7a). There are stronger diurnal variations of $PM_{2.5}$ emission in summer than in
293 winter, which are represented by larger $PM_{2.5}$ emission fractions during morning and less $PM_{2.5}$
294 emission fractions during evening. The diurnal variations of $PM_{2.5}$ emission from March to May
295 gradually transform from the patterns of winter to those of summer, and *vice versa* for the diurnal
296 variations of $PM_{2.5}$ emission from September to November. The monthly changes of diurnal
297 variations of $PM_{2.5}$ emission are consistent with the seasonal dependence, since monthly variations
298 of $PM_{2.5}$ emission are mainly related to the variations of residential consumptions (Li et al., 2017)
299 in which the space-heating has nearly no diurnal variations and then larger $PM_{2.5}$ emissions during
300 winter lead to reduced diurnal variations than summer. Similar to the monthly fractions of
301 estimated $PM_{2.5}$ emission for mainland China, diurnal variations of $PM_{2.5}$ emission fraction are
302 consistent cross years for a given month (Figure 8). Table 2 gives five-year mean diurnal variations
303 of the estimated $PM_{2.5}$ emission fraction for each month. Based on these high-resolution diurnal-
304 variation fractions, hourly estimates of $PM_{2.5}$ emission can be objectively obtained for a given
305 monthly estimated $PM_{2.5}$ emission.

306 Despite the high temporal resolution, the DEPE also has the ability to analyze diurnal
307 variations for specific cities. The monthly changes of diurnal variations of $PM_{2.5}$ emission
308 estimated for megacities with urban populations larger than 5 million and non-megacities with
309 urban populations smaller than 5 million (Notice of the State Council on Adjusting the Standards
310 for Categorizing City Sizes, 2014) are consistent with those estimated from mainland China
311 (Figure 7). Compared to the diurnal variations of $PM_{2.5}$ emission estimated for mainland China,
312 the megacities have stronger diurnal variations, while the non-megacities have weaker diurnal

variations. These detailed descriptions of $PM_{2.5}$ emission that are usually absent in common emission estimates can be essential for $PM_{2.5}$ simulation, especially for providing timely and realistic guidance for severe haze events.

There has been lack of local measurements for diurnal variations and widely adopted diurnal variation profiles of $PM_{2.5}$ emission in China. Compared to the diurnal variations of $PM_{2.5}$ emission fractions estimated based on diurnal variation profiles from US and EU (Wang et al., 2010; Du et al., 2020), the estimated $PM_{2.5}$ emission fractions are 1.25% larger during the evening, , which greatly changes the diurnal variations of DEPE. The noon and evening peaks estimated from DEPE have smaller $PM_{2.5}$ emission fractions, with mean underestimations of $PM_{2.5}$ emission fraction of0.40% and 0.83% for noon peak and evening peak respectively (Figures 7a and 9). In fact, the smaller evening peaks of Wang et al. (2010) occurred in November, December, January, February and March, while they are almost indistinct from April to October, similar to that from DEPE. The morning peak of Wang et al. (2010) is similar to that of DEPE for spring and fall, but the former overestimates $PM_{2.5}$ emission fraction of 0.57% for winter while underestimates $PM_{2.5}$ emission fraction of 1.05% for summer. Due to the overestimated peaks, diurnal variations of Wang et al.(2010) have sharper appearance rate for morning peak and disappearance rate for evening peak. Compared to the diurnal variations based on diurnal variation profiles from ES and EU (Wang et al., 2010), the diurnal variations of the DEPE are constrained by the atmospheric-chemical model and observed $PM_{2.5}$ concentrations, which can objectively determine the diurnal variations of $PM_{2.5}$ emission for specific regions and seasons.

5. Impact of COVID-19 on $PM_{2.5}$ emissions

The abrupt changes of $PM_{2.5}$ emissions during the initial stage of COVID-19 in China provide a natural case study to validate the ability of the dynamic-based data assimilation method to obtain high temporal-resolution $PM_{2.5}$ emission estimates. The abrupt outbreak of the COVID-19 pandemic has produced dramatically socioeconomic impacts in China. To prevent the virus spread, a lockdown was first implemented on 23 January 2020 in Wuhan, Hubei province, and subsequently the national lockdown has been enforced in China (Liu et al., 2020; Huang et al., 2020; Zhu et al., 2021). Consequently, the total $PM_{2.5}$ emission of February 2020 for China shows an obvious decrease compared to those of previous years (Figure 3). The high temporal-resolution DEPE reveals the detailed changes of $PM_{2.5}$ emission with time (Figure 10). The $PM_{2.5}$ emission

started to decrease right around the COVID outbreak, and had been smaller than those of year 2019 till early March. The emissions at the following months of 2020 are similar to those of 2019, due to the epidemic prevention and control policies enforced by the China government. During February 2020, the DEPE shows significant reductions at the north China plain and northeast of China where prominent $PM_{2.5}$ emission occurred, while spotted $PM_{2.5}$ emission differences with small magnitudes showed at the other regions (Figures 11a-b). Along with recovery from the COVID-19, the estimated $PM_{2.5}$ emission rebounded in March (Figures 3a, 10, 11c-d), which is contributed to the national work resumption. Thus, the DEPE is able to timely reflect the dynamic response of $PM_{2.5}$ emission to the COVID-19. Although similar emission reductions and emission trends are obtained from the bottom-up technique (Zheng et al., 2021), the reduction amount and ratio from the botomm-up technique are larger than those estimated from DEPE (Figure 10 and Table 1). This is possibly due to significant reductions of $PM_{2.5}$ emission from the residential sector as in the bottom-up techinique (Zheng et al., 2021), however, $PM_{2.5}$ emissions from the residential sector might not significantly changed around the COVID outbreak.

To avoid fluctuations due to diurnal variations and monthly changes of $PM_{2.5}$ emission, 7-day averaged $PM_{2.5}$ emission differences between year 2020 and 2019 are used to analyze the dynamic impact of COVID-19 on $PM_{2.5}$ emission (Figure 12). Before the lockdown, there were slight $PM_{2.5}$ emission differences over several provinces (Figures 12a-b). During the first week of lockdown, $PM_{2.5}$ emission reduction larger than $5x10^{-2}$ ($\mu g \cdot m^{-2} \cdot s^{-1}$) that is about 60%-70% emission reduction, occurred at Hubei, Hunan, Guangdong, Anhui and Zhejiang provinces (Figure 12c). The $PM_{2.5}$ emission reduction extended to BTH and Shandong province during the second week of lockdown (Figure 12d), and continuously spread to the three northeast provinces of China during the third week of lockdown (Figure 12e). During the third week of lockdown, the increased $PM_{2.5}$ emissions for BTH and SCR are possibly caused by the long national vocation of spring holiday of year 2019 (Ji et al., 2018). The inhomogeneous spatial variations of $PM_{2.5}$ emissions possibly relate with different traditions and policy enforcements for different provinces. The $PM_{2.5}$ emission reduction had been maintained over the central and northern China till early March when the lockdown was lift (Figures 12f-i). Though it is hard to see continuous and consistent signal of lockdown for the whole China, the timely DEPE can provide up-to-date guidance for quantifying socioeconomic impacts from rare events with large emission changes such as the COVID-19.

~~Although there were significant reductions of $PM_{2.5}$ emissions over the central and northern China in February 2020, a severe air pollution event occurred over the north China in early February 2020. Previous studies have shown that the factors influencing the severe air pollution event include the still intensive emissions from industrial, power and residential, unfavorable meteorological condition, anomalously high humidity that promoted aerosol heterogeneous chemistry, and secondary aerosol formation associated with increased atmosphere oxidants (Le et al. 2020; Sulaymon et al. 2021; Li et al., 2021) .~~

6. Discussion

High temporal-resolution and dynamics-based estimations of $PM_{2.5}$ emission can be objectively and optimally obtained by assimilating past and future observed surface $PM_{2.5}$ concentrations through flow-dependent error statistics. This advanced assimilation strategy can be applied for emission estimates of other chemical species when corresponding observations are available, and extend to observation types besides the surface concentrations, like the aerosol optical depth (Liu et al., 2011; Choi et al., 2020). Moreover, current estimates of $PM_{2.5}$ emission are lack of explicitly representations of primary and secondary $PM_{2.5}$, which could be resolved by joint estimation of the source emission, primary and secondary $PM_{2.5}$ given the concentration observations. Another deficiency of this top-down technique is that it cannot directly determine dynamics-based $PM_{2.5}$ emissions for different sectors and contributions from different policies, although the bottom-up technique has the potential to untangle the different contributions from different policies and quantify the different impacts on different sectors. However, this top-down technique can be integrated into the bottom-up technique to retain advantages of both methods. One future work is to integrate the top-down technique with the bottom-up one, by which the emission estimates for different sectors and polices could be quantified. The annual emission estimate from the bottom-up technique can be further downscaled to hourly estimates by first distributing the annual amount to each month through the monthly allocations estimated from the top-down technique, and then assuming evenly daily distribution, finally applying the fractions of diurnal variation estimated from the top-down technique. The information collected by the bottom-up technique is retained, while the common drawback of coarse temporal resolution for the bottom-up technique is remedied. The integrated bottom-up and top-down technique can improve spatiotemporal representations of source emissions cross time scales and sectors, which is

beneficial for emission inventory, air quality forecast, regulation policy and emission trading scheme.

Acknowledgments

This work is jointly sponsored by the National Key R&D Program of China through Grant 2017YFC1501603 and the National Natural Science Foundation of China through Grants 41922036 and 42275153. We are grateful to the High Performance Computing Center of Nanjing University for doing the cycling ensemble assimilation experiments.

Data availability

The meteorological data used for meteorological initial conditions and boundary conditions is available from the University Corporation for Atmospheric Research (UCAR) Research Data Archive (https://rda.ucar.edu/datasets/ds083.3/). The assimilated meteorological observations are available from the UCAR Research Data Archive (https://rda.ucar.edu/datasets/ds337.0/), and the assimilated chemical observations are available from https://aqicn.org/map/china/cn/. The prescribed time-invariant anthropogenic emissions are available from the Emission Database for Global Atmospheric Research for Hemispheric Transport of Air Pollution (EDGAR-HTAP) inventory (https://data.jrc.ec.europa.eu/dataset/jrc-edgar-htap_v2-2) and the Multi-resolution Emission Inventory (MEIC; http://meicmodel.org/?page_id=560).

The WRF-Chem model version 3.6.1 is available from https://www2.mmm.ucar.edu/wrf/users/download/get_sources.html#WRF-Chem. The NOAA operational EnKF system is available from https://dtcenter.org/community-code/gridpoint-statistical-interpolation-gsi.

Competing interests

The contact author has declared that none of the authors has any competing interests.

References

Attri, A. K., Kumar, U., and Jain, V. K.: Microclimate: formation of ozone by fireworks, Nature, 411, 1015, 2001.

Barker, D., Huang, X.-Y., Liu, Z., Auligné, T., Zhang, X., Rugg, S., Ajjaji, R., Bourgeois, A., Bray, J., Chen, Y., Demirtas, M., Guo, Y.-R., Henderson, T., Huang, W., Lin, H.-C., Michalakes, J., Rizvi, S., and Zhang, X.: The Weather Research and Forecasting Model's Community Variational/Ensemble Data Assimilation System: WRFDA, B. Am. Meteorol. Soc., 93, 831–843, https://doi.org/10.1175/BAMS-D-11-00167.1, 2012.

Cao, H., Fu, T.-M., Zhang, L., Henze, D. K., Miller, C. C., Lerot, C., Abad, G. G., De Smedt, I., Zhang, Q., van Roozendael, M., Hendrick, F., Chance, K., Li, J., Zheng, J., and Zhao, Y.: Adjoint inversion of Chinese non-methane volatile organic compound emissions using space-based observations of formaldehyde and glyoxal, Atmos. Chem. Phys., 18, 15017–15046, https://doi.org/10.5194/acp-18-15017-2018, 2018.

Chen, C., Dubovik, O., Henze, D. K., Chin, M., Lapyonok, T., Schuster, G. L., Ducos, F., Fuertes, D., Litvinov, P., Li, L., Lopatin, A., Hu, Q., and Torres, B.: Constraining global aerosol emissions using POLDER/PARASOL satellite remote sensing observations, Atmos. Chem. Phys., 19, 14585–14606, https://doi.org/10.5194/acp-19-14585-2019, 2019.

Chin, M., Rood, R. B., Lin, S. J., Muller, J. F., and Thompson, A. M.: Atmospheric sulfur cycle simulated in the global model GO-CART: Model description and global properties, J. Geophys. Res.-Atmos., 105, 24671–24687, 2000.

Choi, Y., Chen, S. H., Huang, C. C., Earl, K., Chen, C. Y., Schwartz, C. S., and Matsui, T.: Evaluating the impact of assimilating aerosol optical depth observations on dust forecasts over North Africa and the East Atlantic using different data assimilation methods, Journal of Advances in Modeling Earth Systems, 12(4), e2019MS001890. https://doi.org/10.1029/2019ms001890, 2020.

Du, Q., Zhao, C., Zhang, M., Dong, X., Chen, Y., Liu, Z., Hu, Z., Zhang, Q., Li, Y., Yuan, R., and Miao, S.: Modeling diurnal variation of surface PM2.5 concentrations over East China with WRF-Chem: impacts from boundary-layer mixing and anthropogenic emission, Atmos. Chem. Phys., 20, 2839–2863, https://doi.org/10.5194/acp-20-2839-2020, 2020.

Elbern, H., Strunk, A., Schmidt, H., and Talagrand, O.: Emission rate and chemical state estimation by 4-dimensional variational inversion, Atmos. Chem. Phys., 7, 3749 – 3769, https://doi.org/10.5194/acp-7-3749-2007, 2007.Gaspari, G. and Cohn S. E.: Construction of correlation functions in two and three dimensions, Q. J. Roy. Meteor. Soc., 125, 723–757, 1999.

Ginoux, P., Chin, M., Tegen, I., Prospero, J. M., Holben, B., Dubovik, O., and Lin, S.-J.: Sources and distributions of dust aerosols simulated with the GOCART model, J. Geophys. Res., 106, 20255–20273, doi:10.1029/2000JD000053, 2001.

Grell, G., Peckham, S. E., Schmitz, R., McKeen, S. A., Frost, G., Skamarock, W. C., and Eder, B.: Fully coupled "online" chem- istry within the WRF model, Atmos. Environ., 39, 6957–6975, https://doi.org/10.1016/j.atmosenv.2005.04.027, 2005.

Guenther, A., Hewitt, C. N., Erickson, D., Fall, R., Geron, C., Graedel, T., Harley, P., Klinger, L., Lerdau, M., McKay, W., Pierce, T., Scholes, B., Steinbrecher, R., Tallamraju, R., Taylor, J., and Zimmerman, P.: A global model of natural volatile organic compound emissions, J. Geophys. Res., 100, 8873–8892, doi:10.1029/94JD02950, 1995.

Huang, X., Ding, A., Gao, J., Zheng, B., Zhou, D., Qi, X., Tang, R., Wang, J., Ren, C., Nie, W., Chi, X., Xu, Z., Chen, L., Li, Y., Che, F., Pang, N., Wang, H., Tong, D., Qin, W., Cheng, W., Liu, W., Fu, Q., Liu, B., Chai, F., Davis, S. J., Zhang, Q., and He, K.: Enhanced secondary pollution offset reduction of primary emissions during COVID-19 lockdown in China, Natl. Sci. Rev., nwaa137, https://doi.org/10.1093/nsr/nwaa137, 2020.

Huang, J., Pan, X. C., Guo, X. B., and Li, G. X.: Health impact of China's Air Pollution Prevention and Control Action Plan: an analysis of national air quality monitoring and mortality data, Lancet Planet. Health, 2, E313–E323, https://doi.org/10.1016/S2542-5196(18)30141-4, 2018.

Janssens-Maenhout, G., Crippa, M., Guizzardi, D., Dentener, F., Muntean, M., Pouliot, G., Keating, T., Zhang, Q., Kurokawa, J., Wankmüller, R., Denier van der Gon, H., Kuenen, J. J. P., Klimont, Z., Frost, G., Darras, S., Koffi, B., and Li, M.: HTAP_v2.2: a mosaic of regional and global emission grid maps for 2008 and 2010 to study hemispheric transport of air pollution, Atmos. Chem. Phys., 15, 11411–11432, https://doi.org/10.5194/acp-15-11411-2015, 2015.

Ji, D., Cui, Y., Li, L., He, J., Wang, L., Zhang, H., Wang, W., Zhou, L., Maenhaut, W., Wen, T., and Wang, Y.: Characterization and source identification of fine particulate matter in urban Beijing during the 2015 Spring Festival, Sci. Total Environ., 628–629, 430–440, https://doi.org/10.1016/j.scitotenv.2018.01.304, 2018.

Jiang, Z., Worden, J. R., Worden, H., Deeter, M., Jones, D. B. A., Arellano, A. F., and Henze, D. K.: A 15-year record of CO emissions constrained by MOPITT CO observations, Atmos. Chem. Phys., 17, 4565–4583, https://doi.org/10.5194/acp-17-4565-2017, 2017.

Kalnay, E.: *Atmospheric* modeling, data assimilation and predictability (p. 341), Cambridge: Cambridge University Press, 2002.

Kleist, D. T., Parrish, D. F., Derber, J. C., Treadon, R., Errico, R. M., and Yang, R.: Improving incremental balance in the GSI 3DVAR analysis system, Mon. Weather Rev., 137, 1046–1060, doi:10.1175/2008MWR2623.1, 2009.

Le, T., Wang, Y., Liu, L., Yang, J., Yung, Y. L., Li, G., and Seinfeld, J. H.: Unexpected air pollution with marked emission reductions during the COVID-19 outbreak in China, Science, 702–706, https://https://doi.org/10.1126/science.abb7431, 2020.

Lei, Y., Zhang, Q., He, K. B., and Streets, D. G.: Primary anthropogenic aerosol emission trends for China, 1990–2005, Atmos. Chem. Phys., 11, 931–954, https://doi.org/10.5194/acp-11-931-2011, 2011.

Li, N., Tang, K., Wang, Y., Wang, J., Feng, W., Zhang, H., Liao, H., Hu, J., Long, X., and Shi, C.: Is the efficacy of satellite-based inversion of SO2 emission model dependent? Environmental Research Letters, 16, 035018, 2021.

Li, K., Jacob, D. J., Liao, H., Zhu, J., Shah, V., Shen, L., Bates, K. H., Zhang, Q., and Zhai, S.: A Two-Pollutant Strategy for Improving Ozone and Particulate Air Quality in China, Nat. Geosci., 12, 906–910, https://doi.org/10.1038/s41561-019-0464-x, 2019a.

Li, J. and Wang, Y.: Inferring the anthropogenic NO_x emission trend over the United States during 2003–2017 from satellite observations: was there a flattening of the emission trend after the Great Recession? Atmos. Chem. Phys., 19, 15339–15352, https://doi.org/10.5194/acp-19-15339-2019, 2019b.

Li, M., Zhang, Q., Kurokawa, J.-I., Woo, J.-H., He, K., Lu, Z., Ohara, T., Song, Y., Streets, D. G., Carmichael, G. R., Cheng, Y., Hong, C., Huo, H., Jiang, X., Kang, S., Liu, F., Su, H., and Zheng, B.: MIX: a mosaic Asian anthropogenic emission inventory under the international collaboration framework of the MICS-Asia and HTAP, Atmos. Chem. Phys., 17, 935–963, https://doi.org/10.5194/acp-17-935-2017, 2017.

Li, M., Zhang, Q., Streets, D. G., He, K. B., Cheng, Y. F., Emmons, L. K., Huo, H., Kang, S. C., Lu, Z., Shao, M., Su, H., Yu, X., and Zhang, Y.: Mapping Asian anthropogenic emissions of non-methane volatile organic compounds to multiple chemical mechanisms, Atmos. Chem. Phys., 14, 5617–5638, https://doi.org/10.5194/acp-14-5617-2014, 2014.

Liu, J., Yin, H., Tang, X., Zhu, T., Zhang, Q., Liu, Z., Tang, X., and Yi, H.: Transition in air pollution, disease burden and health cost in China: A comparative study of long-term and short-term exposure, Environmental Pollution, 277, 116770, 2021.

Liu, T., Wang, X. Y., Hu, J. L., Wang, Q., An, J. Y., Gong, K. J., Sun, J. J., Li, L., Qin, M. M., Li, J. Y., Tian, J. J., Huang, Y. W., Liao, H., Zhou, M., Hu, Q. Y., Yan, R. S., Wang, H. L., and Huang, C.: Driving Forces of Changes in Air Quality during the COVID-19 Lockdown Period in the Yangtze River Delta Region, China, Environ. Sci. Technol., 7, 779–786, https://doi.org/10.1021/acs.estlett.0c00511, 2020.

Liu, T., Cai, Y., Feng, B., Cao, G., Lin, H., Xiao, J., Li, X., Liu, S., Pei, L., Fu, L., Yang, X., and Zhang, B.: Long-term mortality benefits of air quality improvement during the twelfth five-year-plan period in 31 provincial capital cities of China, Atmospheric Environment, 173, 53–61, https://doi.org/10.1016/j.atmosenv.2017.10.054, 2018.

Liu, Z., Liu, Q., Lin, H. C., Schwartz, C. S., Lee, Y. H., andWang, T.: Three-dimensional variational assimilation of MODISaerosol optical depth: implementation and application to a dust storm over East Asia, J. Geophys. Res., 116, D23206,https://doi.org/10.1029/2011JD016159, 2011.

Miyazaki, K., Bowman, K., Sekiya, T., Eskes, H., Boersma, F., Worden, H., Livesey, N., Payne, V. H., Sudo, K., Kanaya, Y., Takigawa, M., and Ogochi, K.: Updated tropospheric chemistry reanalysis and emission

estimates, TCR-2, for 2005–2018, Earth Syst. Sci. Data, 12, 2223–2259, https://doi.org/10.5194/essd-12-2223-2020, 2020.

Miyazaki, K., Eskes, H., Sudo, K., Boersma, K. F., Bowman, K., and Kanaya, Y.: Decadal changes in global surface NO_x emissions from multi-constituent satellite data assimilation, Atmos. Chem. Phys., 17, 807–837, https://doi.org/10.5194/acp-17-807-2017, 2017.

Müller, J.-F., Stavrakou, T., Bauwens, M., George, M., Hurtmans, D., Coheur, P.-F., Clerbaux, C., and Sweeney, C.: Top-Down CO Emissions Based on IASI Observations and Hemispheric Constraints on OH Levels, Geophys. Res. Lett., 45, 1621–1629, https://doi.org/10.1002/2017GL076697, 2018.

Notice of the State Council on Adjusting the Standards for Categorizing City Sizes (in Chinese) (Chinese State Council, 2014); http://www.gov.cn/zwgk/2013-09/12/content_2486773.htm

Peng, Z., Lei, L., Liu, Z., Liu, H., Chu, K., and Kou, X.: Impact of Assimilating Meteorological Observations on Source Emissions Estimate and Chemical Simulations, Geophys. Res. Lett., 47, e2020GL089030, https://doi.org/10.1029/2020GL089030, 2020.

Peng, Z., Lei, L., Liu, Z., Sun, J., Ding, A., Ban, J., Chen, D., Kou, X., and Chu, K.: The impact of multi-species surface chemical observation assimilation on air quality forecasts in China, Atmos. Chem. Phys., 18, 17387–17404, https://doi.org/10.5194/acp-18-17387-2018, 2018.

Peng, Z., Liu, Z., Chen, D., and Ban, J.: Improving $PM_{2.5}$ forecast over China by the joint adjustment of initial conditions and source emissions with an ensemble Kalman filter, Atmos. Chem. Phys., 17, 4837–4855, https://doi.org/10.5194/acp-17-4837-2017, 2017.

Peng, Z., Zhang, M., Kou, X., Tian, X., and Ma, X.: A regional carbon data assimilation system and its preliminary evaluation in East Asia, Atmos. Chem. Phys., 15, 1087–1104, https://doi.org/10.5194/acp-15-1087-2015, 2015.

Peters, W., Jacobson, A. R., Sweeney, C., Andrews, A. E., Conway, T. J., Masarie, K., Miller, J. B., Bruhwiler, L. M. P., Petron, G., Hirsch, A. I.,Worthy, D. E. J., van derWerf, G. R., Randerson, J. T.,Wennberg, P. O., Krol, M. C., and Tans, P. P.: An atmospheric perspective on North American carbon dioxide exchange: CarbonTracker, P. Natl. Acad. Sci. USA, 104, 18925–18930, 2007.

Qu, Z., Henze, D. K., Capps, S. L., Wang, Y., Xu, X., and Wang, J.: Monthly top-down NOx emissions for China (2005–2012): a hybrid inversion method and trend analysis, J. Geophys. Res., 122, 4600–4625, https://doi.org/10.1002/2016JD025852, 2017.

Streets, D. G., Bond, T. M. L., Carmichael, G. R., Fernandes, S., Fu, Q., He, D., Klimont, Z., Nelson, S. M., Tsai, N. Y., Wang, M. Q., Woo, J.-H., and Yarber, K. F.: An inventory of gaseous and primary aerosol emissions in Asia in the year 2000. J. Geophys. Res., 108(D21), 8809, doi:10.1029/2002JD003093, 2003.

Sulaymon et al. 2021. Persistent high PM2.5 pollution driven by unfavorable meteorological conditions during the COVID-19 lockdown period in the Beijing-Tianjin-Hebei region, China. Environmental Research. https://doi.org/10.1016/j.envres.2021.111186

Torn, R. D., Hakim, G. J., and Snyder, C.: Boundary conditions forlimited-area ensemble Kalman filters, Mon. Weather Rev., 134,2490–2502, 2006.

Wang, H., He, X., Liang, X., Choma, E. F., Liu, Y., Shan, L., Zheng, H., Zhang, S., Nielsen, C. P., Wang, S., Wu, Y., and Evans, J. S.: Health benefits of on-road transportation pollution control programs in China, P. Natl. Acad. Sci. USA, 117, 25370, https://doi.org/10.1073/pnas.1921271117, 2020.

Wang, G., Cheng, S. Y., Wei, W., Yang, X. W., Wang, X. Q. Jia, J., Lang, J. L., and Lv, Z.: Characteristics and emission reduction measures evaluation of PM2.5 during the two major events: APEC and Parade, Sci. Total Environ., 595, 81–92, https://doi.org/10.1016/j.scitotenv.2017.03.231, 2017.

Wang, Z., Li, J., Wang, Z., Yang, W., Tang, X., Ge, B., Yan, P., Zhu, L., Chen, X., and Chen, H.: Modeling study of regional severe hazes over mid-eastern China in January 2013 and its implica- tions on pollution prevention and control, Sci. China-Earth Sci.,57, 3–13, 2014.

Wang, X. Y., Liang, X. Z., Jiang, W. M., Tao, Z. N., Wang, J. X. L., Liu, H. N., Han, Z. W., Liu, S. Y., Zhang, Y. Y., Grell, G. A., and Peckham, S. E.: WRF-Chem simulation of East Asian air quality: Sensitivity to temporal and vertical emissions distributions, Atmos. Environ., 44, 660–669, 2010.

Whitaker, J. S. and Hamill, T. M.: Ensemble data assimilation without perturbed observations, Mon. Weather Rev., 130, 1913–1924,2002.

Whitaker, J. S. and Hamill, T. M.: Evaluating methods to account for system errors in ensemble data assimilation, Mon. Weather Rev., 140, 3078–3089, 2012.

Yang, Y., Ren, L., Li, H., Wang, H., Wang, P., Chen, L., Yue, X., and Liao, H.: Fast climate responses to aerosol emission reductions during the COVID-19 pandemic, Geophys. Res. Lett., 47, e2020GL089788, https://doi.org/10.1029/2020gl089788, 2020.

Zhai, S., Jacob, D. J., Wang, X., Liu, Z., Wen, T., Shah, V., Li, K., Moch, J. M., Bates, K. H., Song, S., Shen, L., Zhang, Y., Luo, G., Yu, F., Sun, Y., Wang, L., Qi, M., Tao, J., Gui, K., Xu, H., Zhang, Q., Zhao, T., Wang, Y., Lee, H. C., Choi, H., and Liao, H.: Control of particulate nitrate air pollution in China, Nat. Geosci., 14, 1–7, 2021.

Zhang, Q., Zheng, Y., Tong, D., Shao, M., Wang, S., Zhang, Y., Xu, X., Wang, J., He, H., Liu, W., Ding, Y., Lei, Y., Li, J., Wang, Z., Zhang, X., Wang, Y., Cheng, J., Liu, Y., Shi, Q., Yan, L., Geng, G., Hong, C., Li, M., Liu, F., Zheng, B., Cao, J., Ding, A., Gao, J., Fu, Q., Huo, J., Liu, B., Liu, Z., Yang, F., He, K., and Hao, J.: Drivers of Improved $PM_{2.5}$ Air Quality in China from 2013 to 2017, P. Natl. Acad. Sci. USA, 116, 24463–24469, https://doi.org/10.1073/pnas.1907956116, 2019.

Zhang, L., Shao, J. Y., Lu, X., Zhao, Y. H., Hu, Y. Y., Henze, D. K., Liao, H., Gong, S., and Zhang, Q.: Sources and processes affect-ing fine particulate matter pollution over North China: An adjoint analysis of the Beijing APEC period, Environ. Sci. Technol., 50,8731–8740, https://doi.org/10.1021/acs.est.6b03010, 2016.

Zhang, Q., Streets, D. G., Carmichael, G. R., He, K. B., Huo, H., Kannari, A., Klimont, Z., Park, I. S., Reddy, S., Fu, J. S., Chen, D., Duan, L., Lei, Y., Wang, L. T., and Yao, Z. L.: Asian emis- sions in 2006 for the

NASA INTEX-B mission, Atmos. Chem. Phys., 9, 5131–5153, https://doi.org/10.5194/acp-9-5131-2009, 2009.

Zheng, B., Zhang, Q., Geng, G., Chen, C., Shi, Q., Cui, M., Lei, Y., and He, K.: Changes in China's anthropogenic emissions and air quality during the COVID-19 pandemic in 2020, Earth Syst. Sci. Data, 13, 2895–2907, https://doi.org/10.5194/essd-13-2895-2021, 2021.

Zheng, B., Geng, G., Ciais, P., Davis, S. J., Martin, R. V., Meng, J., Wu, N., Chevallier, F., Broquet, G., Boersma, F., van der A, R., Lin, J., Guan, D., Lei, Y., He, K., and Zhang, Q.: Satellite-based estimates of decline and rebound in China's CO_2 emissions during COVID-19 pandemic, Sci. Adv., 6, eabd4998, https://doi.org/10.1126/sciadv.abd4998, 2020.

Zheng, B., Tong, D., Li, M., Liu, F., Hong, C., Geng, G., Li, H., Li, X., Peng, L., Qi, J., Yan, L., Zhang, Y., Zhao, H., Zheng, Y., He, K., and Zhang, Q.: Trends in China's anthropogenic emissions since 2010 as the consequence of clean air actions, Atmos. Chem. Phys., 18, 14095–14111, https://doi.org/10.5194/acp-18-14095-2018, 2018.

Zhu, J., Chen, L., Liao, H., Yang, H., Yang, Y., and Yue, X.: Enhanced $PM_{2.5}$ Decreases and O_3 Increases in China during COVID-19 Lockdown by Aerosol-Radiation Feedback, Geophys. Res. Lett., 48, e2020GL090260, https://doi.org/10.1029/2020GL090260, 2021.

Figures and Tables

Captions:

Figure 1. Times series of hourly $PM_{2.5}$ concentration biases ($\mu g \cdot m^{-3}$). The ensemble mean priors compared to the observed quantities for December of years 2016-2020 (gray and black), and the mean biases of years 2016-2020 (blue).

Figure 2. Model domain and observation sites for cycling assimilation. Red and blue dots denote the assimilated and unassimilated observational sites, respectively.

Figure 3. (a) Dynamics-based monthly $PM_{2.5}$ emission estimates ($Tg \cdot day^{-1}$) summed over mainland China of each year from 2016 to 2020 (colored) and the estimated $PM_{2.5}$ emission from MEIC (gray); (b) Ratio of $PM_{2.5}$ emission changes between two adjacent years from year 2016 to 2020 normalized by the $PM_{2.5}$ emission of year 2016; (c) Monthly fractions of dynamics-based $PM_{2.5}$ emission estimates for years 2016-2020 (light blue), the five-year mean fractions of dynamics-based monthly $PM_{2.5}$ emission estimates with bars denoting one standard deviation of the five-year variations (dark blue), and the monthly fractions of estimated $PM_{2.5}$ emission from MEIC (gray).

Figure 4. (a) Spatial distribution of dynamics-based $PM_{2.5}$ emission estimates ($\mu g \cdot m^{-2} \cdot s^{-1}$) for year 2016, and compared to that of year 2016, spatial distributions of dynamics-based $PM_{2.5}$ emission changes of year (b) 2017, (c) 2018, (d) 2019 and (e) 2020.

Figure 5. (a) The differences of dynamics-based $PM_{2.5}$ emission estimates between years 2017-2020 and 2016, and (b) the differences normalized by that of year 2016.

Figure 6. Spatial distributions of dynamics-based $PM_{2.5}$ emission changes in December compaered to November in (a) December 2017 compared to November 2017 and (b) December 2018 compared to November 2018. ~~(a) 2017 and (b) 2018~~.

Figure 7. Five-year mean diurnal variations of dynamics-based $PM_{2.5}$ emission fraction averaged over (a) mainland China, (b) megacities with urban population ≥ 5 million, and (c) non-megacities with urban population < 5 million.

Figure 8. Diurnal variations of dynamics-based $PM_{2.5}$ emission fractions for years 2016-2020 (light blue) and five-year mean fractions with bars denoting one standard deviation of the five-year variations (dark blue) are averaged over mainland China for (a) January, (b) April, (c) July, and (d) October.

Figure 9. Diurnal variations of $PM_{2.5}$ emission fraction for each month based on diurnal variation profiles from ES and EU (Wang et al. 2010).

Figure 10. Hourly (light red and blue) and daily (dark red and blue) dynamics-based $PM_{2.5}$ emission estimates ($kg \cdot h^{-1}$) summed over mainland China from January to March of years 2019 and 2020.

Figure 11. Spatial distributions of dynamics-based $PM_{2.5}$ emission estimates ($\mu g \cdot m^{-2} \cdot s^{-1}$) on (~~b~~a) February and (~~d~~c) March of year 2019, and spatial distributions of dynamics-based $PM_{2.5}$ emission reduction of year 2020 compared to year 2019 for (~~c~~b) February and (~~e~~d) March.

Figure 12. Mean spatial distributions of $PM_{2.5}$ emission differences ($\mu g \cdot m^{-2} \cdot s^{-1}$) between year 2020 and 2019 for 9 weeks starting at 9 January 2020. Negative (positive) values indicate that $PM_{2.5}$ emission of year 2020 is smaller (larger) than that of year 2019. The numbers in (a) denote provinces as: 1 Heilongjiang, 2 Neimenggu, 3 Xinjiang, 4 Jilin, 5 Liaoning, 6 Gansu, 7 Hebei, 8 Beijing, 9 Shanxi, 10 Tianjin, 11 Shanxi, 12 Ningxia, 13 Qinghai, 14 Shandong, 15 Xizang, 16 Henan, 17 Jiangsu, 18 Anhui, 19 Sichuan, 20 Hubei, 21 Chongqing, 22 Shanghai, 23 Zhejiang, 24 Hunan, 25 Jiangxi, 26 Yunnan, 27 Guizhou, 28 Fujian, 29 Guangxi, 30 Guangdong, 31 Taiwan, 32 Hongkong, 33 Macao, 34 Hainan.

带格式的: 两端对齐, 行距: 1.5 倍行距

Table 1. Dynamics-based $PM_{2.5}$ emission estimates of year 2016 for each province whose value is larger than 0.01 $\mu g \cdot m^{-2} \cdot s^{-1}$ are shown in the second column. Ratios of $PM_{2.5}$ emission changes of years 2017-2020 compared to year 2016 are shown from the third to the sixth column, with negative (positive) values indicating decrease (increase) of $PM_{2.5}$ emission.

Table 2. Five-year mean diurnal fractions (%) of the dynamics-based $PM_{2.5}$ emission estimates over mainland China on local solar time (LST) for each month.

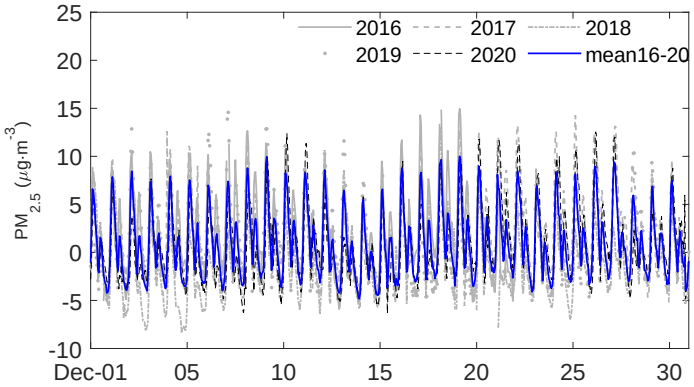

Figure 1. Times series of hourly $PM_{2.5}$ concentration biases ($\mu g \cdot m^{-3}$). The ensemble mean priors compared to the observed quantities for December of years 2016-2020 (gray and black), and the mean biases of years 2016-2020 (blue).

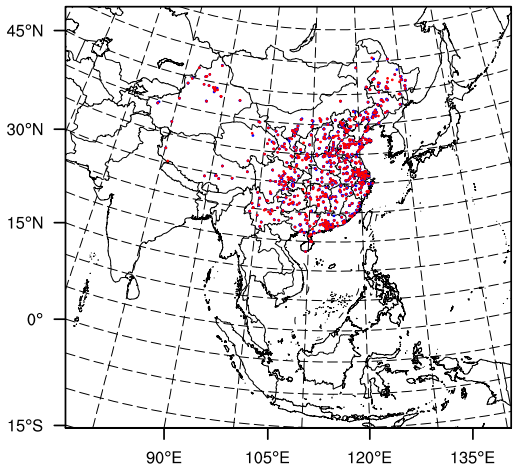

Figure 2. Model domain and observation sites for cycling assimilation. Red and blue dots denote the assimilated and unassimilated observational sites, respectively.

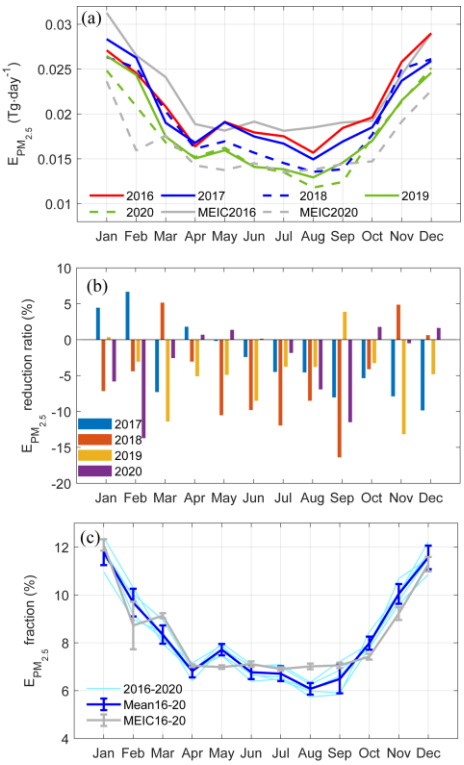

Figure 3. (a) Dynamics-based monthly $PM_{2.5}$ emission estimates (Tg·day^{-1}) summed over mainland China of each year from 2016 to 2020 (colored) and the estimated $PM_{2.5}$ emission from MEIC (gray); (b) Ratio of $PM_{2.5}$ emission changes between two adjacent years from year 2016 to 2020 normalized by the $PM_{2.5}$ emission of year 2016; (c) Monthly fractions of dynamics-based $PM_{2.5}$ emission estimates for years 2016-2020 (light blue), the five-year mean fractions of dynamics-based monthly $PM_{2.5}$ emission estimates with bars denoting one standard deviation of the five-year variations (dark blue), and the monthly fractions of estimated $PM_{2.5}$ emission from MEIC (gray).

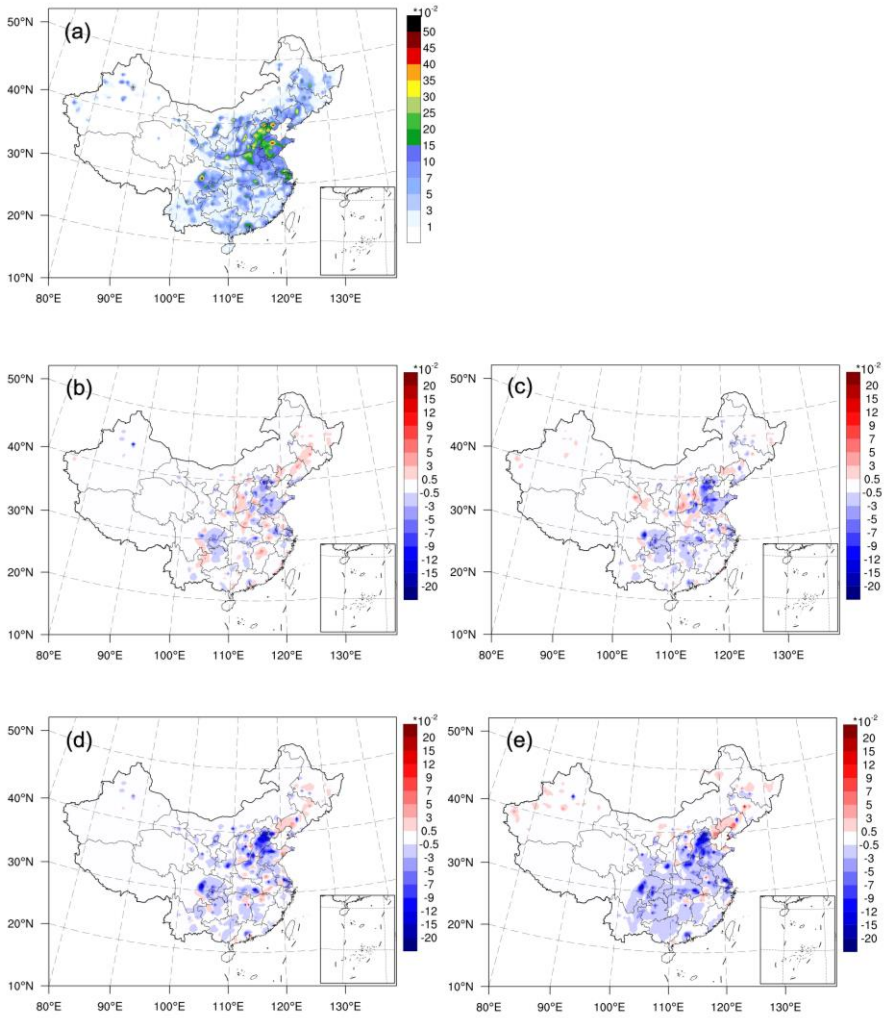

Figure 4. (a) Spatial distribution of dynamics-based $PM_{2.5}$ emission estimates ($\mu g \cdot m^{-2} \cdot s^{-1}$) for year 2016, and compared to that of year 2016, spatial distributions of dynamics-based $PM_{2.5}$ emission changes of year (b) 2017, (c) 2018, (d) 2019 and (e) 2020.

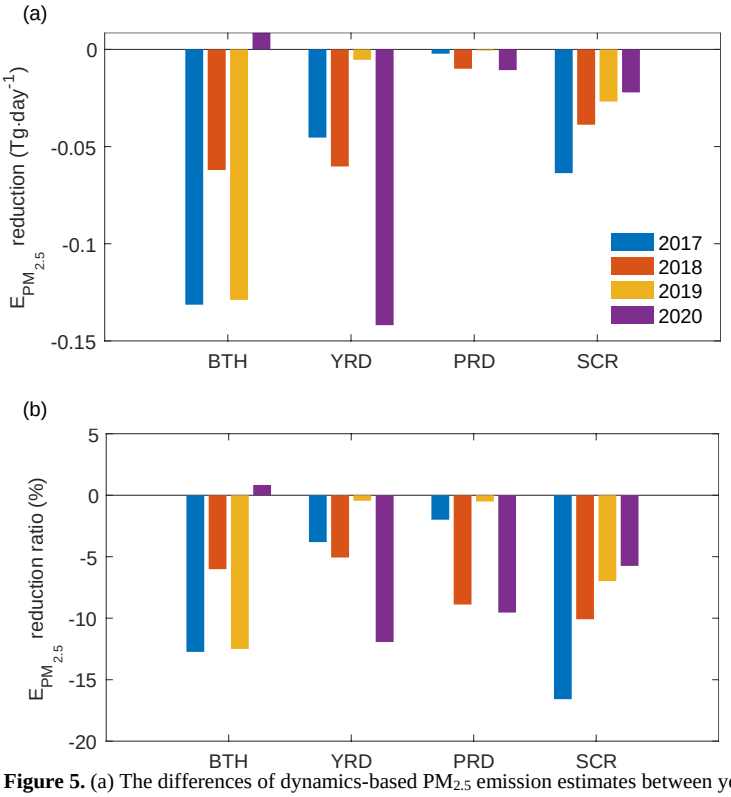

Figure 5. (a) The differences of dynamics-based $PM_{2.5}$ emission estimates between years 2017-2020 and 2016, and (b) the differences normalized by that of year 2016.

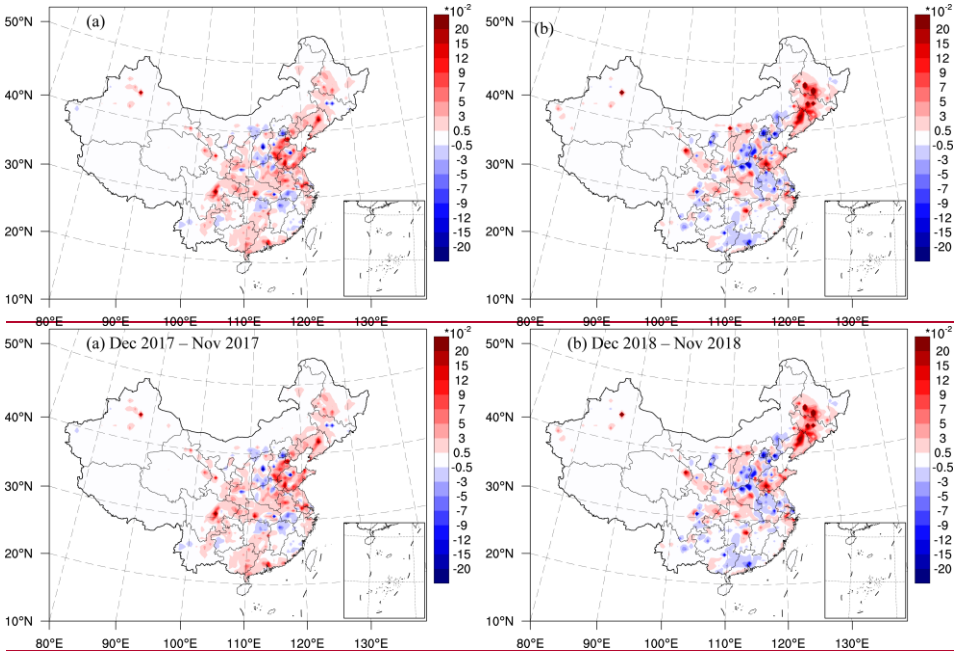

Figure 6. Spatial distributions of dynamics-based $PM_{2.5}$ emission changes in (a) December 2017 compared to November 2017 ~~in (a) 2017~~ and (b) December 2018 compared to November 2018.

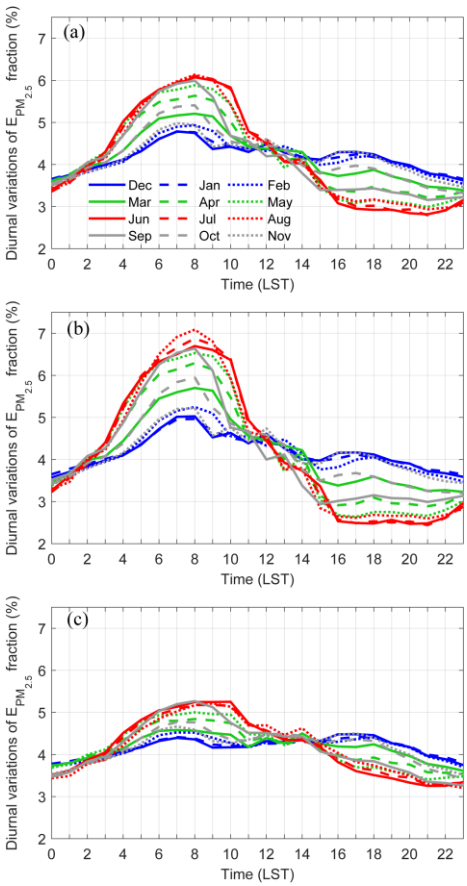

Figure 7. Five-year mean diurnal variations of dynamics-based $PM_{2.5}$ emission fraction averaged over (a) mainland China, (b) megacities with urban population ≥ 5 million, and (c) non-megacities with urban population < 5 million.

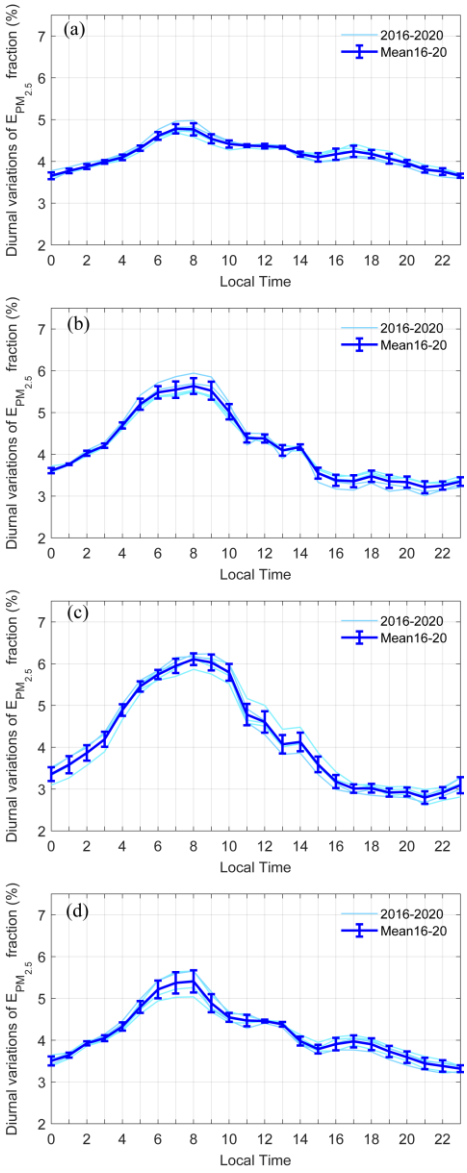

Figure 8. Diurnal variations of dynamics-based $PM_{2.5}$ emission fractions for years 2016-2020 (light blue) and five-year mean fractions with bars denoting one standard deviation of the five-year variations (dark blue) are averaged over mainland China for (a) January, (b) April, (c) July, and (d) October.

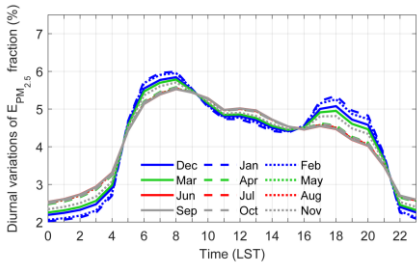

Figure 9. Diurnal variations of $PM_{2.5}$ emission fraction for each month based on diurnal variation profiles from ES and EU (Wang et al. 2010).

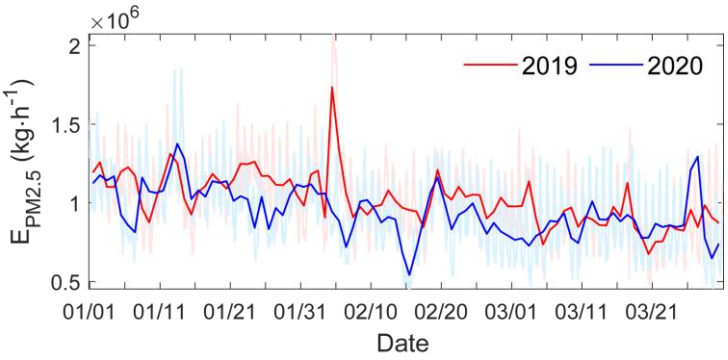

Figure 10. Hourly (light red and blue) and daily (dark red and blue) dynamics-based $PM_{2.5}$ emission estimates ($kg \cdot h^{-1}$) summed over mainland China from January to March of years 2019 and 2020.

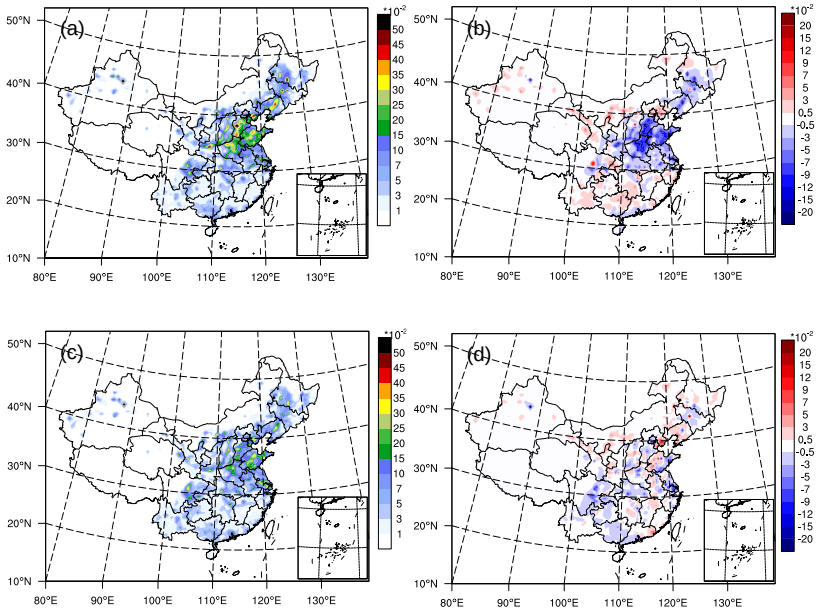

Figure 11. Spatial distributions of dynamics-based $PM_{2.5}$ emission estimates ($\mu g \cdot m^{-2} \cdot s^{-1}$) on (~~b~~a) February and (~~d~~c) March of year 2019, and spatial distributions of dynamics-based $PM_{2.5}$ emission reduction of year 2020 compared to year 2019 for (~~e~~b) February and (~~e~~d) March.

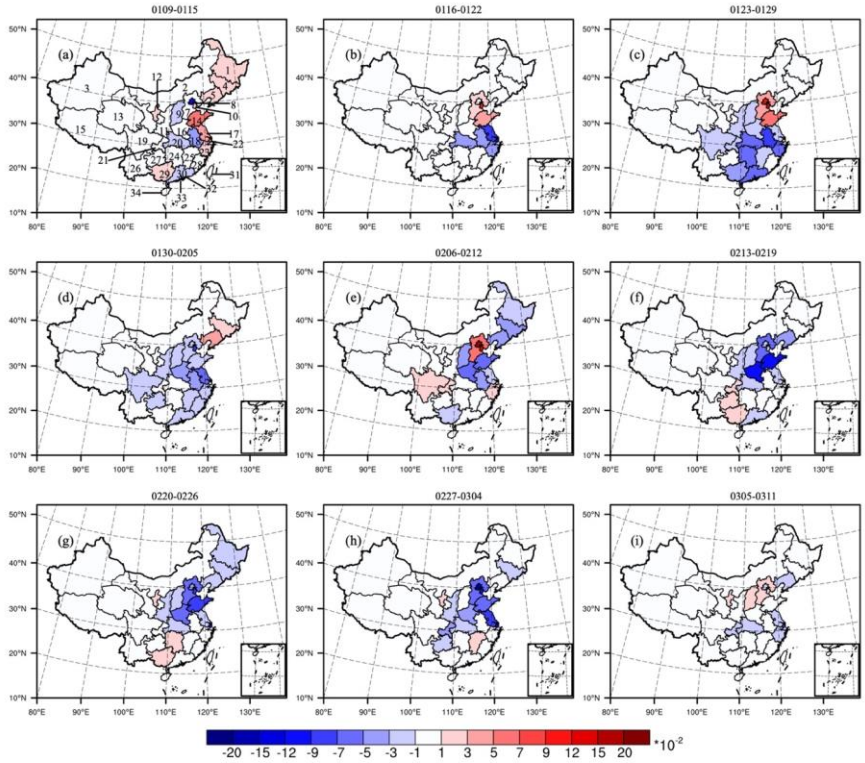

Figure 12. Mean spatial distributions of $PM_{2.5}$ emission differences ($\mu g \cdot m^{-2} \cdot s^{-1}$) between year 2020 and 2019 for 9 weeks starting at 9 January 2020. Negative (positive) values indicate that $PM_{2.5}$ emission of year 2020 is smaller (larger) than that of year 2019. The numbers in (a) denote provinces as: 1 Heilongjiang, 2 Neimenggu, 3 Xinjiang, 4 Jilin, 5 Liaoning, 6 Gansu, 7 Hebei, 8 Beijing, 9 Shanxi, 10 Tianjin, 11 Shanxi, 12 Ningxia, 13 Qinghai, 14 Shandong, 15 Xizang, 16 Henan, 17 Jiangsu, 18 Anhui, 19 Sichuan, 20 Hubei, 21 Chongqing, 22 Shanghai, 23 Zhejiang, 24 Hunan, 25 Jiangxi, 26 Yunnan, 27 Guizhou, 28 Fujian, 29 Guangxi, 30 Guangdong, 31 Taiwan, 32 Hongkong, 33 Macao, 34 Hainan.

Table 1. Dynamics-based $PM_{2.5}$ emission estimates of year 2016 for each province whose value is larger than 0.01 $\mu g \cdot m^{-2} \cdot s^{-1}$ are shown in the second column. Ratios of $PM_{2.5}$ emission changes of years 2017-2020 compared to year 2016 are shown from the third to the sixth column, with negative (positive) values indicating decrease (increase) of $PM_{2.5}$ emission.

Province	$PM_{2.5}$ emission of year 2016 ($\mu g \cdot m^{-2} \cdot s^{-1}$)	Percentage of $PM_{2.5}$ emission change for year 2017 (%)	Percentage of $PM_{2.5}$ emission change for year 2018 (%)	Percentage of $PM_{2.5}$ emission change for year 2019 (%)	Percentage of $PM_{2.5}$ emission change for year 2020 (%)
Tianjin	0.2083	-14.07	-22.99	-38.70	-26.98
Shanghai	0.2067	-24.39	-30.21	-21.46	-30.05
Shandong	0.1631	-15.26	-21.02	-15.57	-19.41
Beijing	0.1598	-26.64	-25.75	-41.92	-45.27
Hebei	0.1178	-7.47	-11.98	-26.39	-22.87
Jiangsu	0.1088	-6.52	-3.98	-12.69	-28.20
Henan	0.1064	-1.41	-3.68	-12.15	-24.91
Shanxi	0.0885	6.17	7.90	-13.18	-13.85
Liaoning	0.0742	6.32	-2.58	3.22	11.42
Anhui	0.0687	1.92	-5.63	-6.23	-21.57
Hubei	0.0574	-5.87	-17.69	-19.76	-36.48
Zhejiang	0.0557	-3.62	-9.32	-9.99	-18.05
Chongqing	0.0525	-22.24	-29.81	-24.63	-38.41
Shanxi	0.0498	0.62	-1.97	-18.05	-17.85
Guangdong	0.0481	1.21	-6.01	-6.69	-14.37
Ningxia	0.0481	-8.17	-5.93	-24.46	-12.95
Hunan	0.0417	-6.40	-19.35	-9.91	-20.62
Guangxi	0.0390	-2.42	-3.52	-12.47	-22.31
Guizhou	0.0365	-4.01	-15.82	-21.74	-46.41
Jilin	0.0360	12.30	-3.22	7.37	4.76
Jiangxi	0.0353	13.22	-9.67	-7.19	-11.91
Sichuan	0.0337	-7.66	-15.66	-27.68	-37.93
Fujian	0.0244	3.13	-2.73	-8.13	-13.41
Heilongjiang	0.0231	7.30	-0.21	3.14	3.91
Yunnan	0.0221	-1.26	-7.16	-9.93	-15.35
Gansu	0.0177	-4.26	5.28	-17.89	-16.49
Hainan	0.0173	3.93	-0.41	-5.04	-4.78
Neimenggu	0.0141	-0.00	-3.63	-8.16	3.55

Table 2. Five-year mean diurnal fractions (%) of the dynamics-based $PM_{2.5}$ emission estimates over mainland China on local solar time (LST) for each month.

	Jan	Feb	Mar	Apr	May	Jun	Jul	Aug	Sep	Oct	Nov	Dec
0	3.65	3.58	3.61	3.61	3.55	3.40	3.36	3.44	3.55	3.50	3.53	3.63
1	3.77	3.69	3.72	3.76	3.74	3.65	3.58	3.56	3.70	3.64	3.64	3.75
2	3.88	3.82	3.96	4.03	4.05	3.94	3.86	4.01	4.05	3.93	3.83	3.89
3	3.98	3.94	4.05	4.21	4.29	4.30	4.19	4.14	4.19	4.05	3.93	3.99
4	4.10	4.06	4.33	4.69	4.92	5.03	4.89	4.71	4.69	4.33	4.12	4.12
5	4.32	4.38	4.76	5.20	5.46	5.48	5.45	5.39	5.27	4.80	4.45	4.32
6	4.61	4.74	5.09	5.48	5.72	5.78	5.74	5.78	5.74	5.21	4.83	4.61
7	4.78	4.90	5.17	5.55	5.78	5.92	5.95	5.98	5.92	5.37	4.98	4.79
8	4.77	4.93	5.21	5.63	5.88	6.07	6.11	6.13	5.99	5.41	4.94	4.75
9	4.54	4.79	5.14	5.52	5.79	6.00	6.03	6.02	5.60	4.89	4.42	4.37
10	4.41	4.41	4.68	5.02	5.43	5.83	5.79	5.42	4.68	4.55	4.50	4.42
11	4.38	4.40	4.42	4.39	4.45	4.79	4.78	4.66	4.56	4.47	4.36	4.30
12	4.37	4.32	4.37	4.38	4.48	4.49	4.61	4.51	4.19	4.46	4.60	4.48
13	4.34	4.43	4.34	4.09	3.93	4.06	4.07	4.09	4.23	4.38	4.33	4.29
14	4.17	4.26	4.30	4.18	4.16	4.02	4.13	4.10	3.79	3.98	4.10	4.15
15	4.10	3.99	3.82	3.55	3.46	3.63	3.59	3.45	3.39	3.79	4.07	4.12
16	4.17	4.05	3.73	3.38	3.17	3.08	3.18	3.24	3.40	3.92	4.30	4.29
17	4.24	4.17	3.79	3.36	3.08	2.95	3.01	3.12	3.41	3.98	4.31	4.30
18	4.18	4.21	3.87	3.48	3.16	2.92	3.03	3.17	3.44	3.91	4.21	4.24
19	4.06	4.04	3.72	3.35	3.12	2.92	2.93	3.08	3.34	3.73	3.99	4.07
20	3.96	3.93	3.62	3.34	3.07	2.84	2.93	3.04	3.29	3.59	3.85	3.98
21	3.81	3.75	3.47	3.21	2.99	2.83	2.80	2.93	3.16	3.44	3.65	3.79
22	3.76	3.66	3.44	3.25	3.09	2.91	2.92	2.97	3.19	3.38	3.56	3.73
23	3.65	3.55	3.39	3.34	3.23	3.16	3.09	3.04	3.23	3.32	3.47	3.62

Appendix: Effects of meteorology

An observing system simulation experiment (OSSE) is performed to investigate the effects of time-varying boundary layer. A nature run is first conducted from 0000 UTC 25 December 2015 to 0000 UTC 2 February 2016, forced by the time invariant source emissions PR2010 (the true emission). Synthetic observations of the six conventional air pollutant concentrations (i.e., PM_{10}, $PM_{2.5}$, SO_2, NO_2, O_3, and CO) are generated from the natural run. Hourly synthetic observations are created from 0000 UTC 29 December 2015 to 0006 UTC 1 February 2016, by interpolating the gridded true surface concentrations to the chemical observation locations with additive random errors of $N(0,R)$. R is the observation error variance, which is calculated by the formula in Elbern et al. (2007). Outputs from the first four days of the natural run are excluded to avoid the transient effect. Then the prior emissions are generated by $F^{pr} = (1.8 + \delta(x,y,z,t))F^{tr}$, where F^{tr} is the true emission, δ is a random number sampled from the normal distribution $N(0,1)$ (Peng et al. 2015). Ensemble data assimilation experiments are conducted from 0000 UTC 29 December to 0006 UTC 1 February 2016. Outputs from the first two days of the OSSE are excluded due to the spin-up.

The magnitude of posterior $PM_{2.5}$ emission is closer to the true emission than the prior. Figure S1 presents the monthly mean diurnal variations of $PM_{2.5}$ emission fraction from the OSSE. It shows that a little larger estimated $PM_{2.5}$ emission fractions occurred in the morning and smaller estimated $PM_{2.5}$ emission fractions occurred in the afternoon, comparing to the time-invariant true emission. But the diurnal variations of $PM_{2.5}$ emission fractions caused by the boundary layer are not as strong as that caused by the emission itself (Figure 7). The reason may be that we have hourly assimilated observations to simultaneously update the chemical concentrations and source emissions. Therefore, the impacts of time-varying boundary layer on the posterior $PM_{2.5}$ emissions are limited.

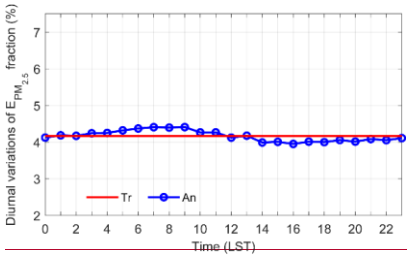

Figure S1. Diurnal variations of $PM_{2.5}$ emission fraction for the Observing System Simulation Experiment.